Moiré patterns and inversion boundaries in graphene/hexagonal boron nitride bilayers

K. R. Elder [1], Zhi-Feng Huang [2], and Tapio Ala-Nissila [3,4,5]

[1]*Department of Physics, Oakland University, Rochester, Michigan 48309, USA*

[2]*Department of Physics and Astronomy, Wayne State University, Detroit, Michigan 48201, USA*

[3]*Department of Applied Physics, QTF Centre of Excellence, Aalto University School of Science, P.O. Box 11000, FI-00076 Aalto, Espoo, Finland*

[4]*Department of Physics, P.O. Box 1843, Brown University, Providence, Rhode Island 02912-1843, USA*

[5]*Department of Mathematical Sciences, Interdisciplinary Centre for Mathematical Modelling, Loughborough University, Loughborough, Leicestershire LE11 3TU, United Kingdom*

(Received 30 November 2022; accepted 23 January 2023; published 8 February 2023)

In this paper a systematic examination of graphene/hexagonal boron nitride (g/hBN) bilayers is presented, through a recently developed two-dimensional phase field crystal model that incorporates out-of-plane deformations. The system parameters are determined by closely matching the stacking energies and heights of g/hBN bilayers to those obtained from existing quantum-mechanical density functional theory calculations. Out-of-plane deformations are shown to reduce the energies of inversion domain boundaries in hBN, and the coupling between graphene and hBN layers leads to a bilayer defect configuration consisting of an inversion boundary in hBN and a domain wall in graphene. Simulations of twisted bilayers reveal the structure, energy, and elastic properties of the corresponding moiré patterns and show a crossover as the misorientation angle between the layers increases from a well-defined hexagonal network of domain boundaries and junctions to smeared-out patterns. The transition occurs when the thickness of domain walls approaches the size of the moiré patterns and coincides with the peaks in the average von Mises and volumetric stresses of the bilayer.

DOI: 10.1103/PhysRevMaterials.7.024003

I. INTRODUCTION

Two-dimensional (2D) materials, such as graphene (g), hexagonal boron nitride (hBN), and transition-metal dichalcogenides (TMDs), have been of continuously great interest in recent years due to their extraordinary electronic, thermal, and mechanical properties, and potential for various technological applications [1,2]. Currently there has been a focus on stacking of such materials together to form multiple-layer structures with tunable physical properties. Perhaps the simplest of such systems, namely, a graphene bilayer, has long shown interesting behavior ranging from being a good insulator to a superconductor [3,4], whereas the stacking of an hBN layer onto a graphene monolayer significantly increases thermal conductivity [5]. Many other exotic features, particularly, those arising from the modulation of novel electronic properties, such as fractal quantum Hall effects in g/hBN bilayers [6–9], have also been reported.

An important feature of bilayer heterostructures is the emergence of moiré patterns or superlattices which play a key role in determining the material properties described above, given their long-range superstructural behavior of periodic structural and electronic modulations coupled with the underlying short-range atomic-scale lattice or sublattice structure [6,7]. Moiré patterns in g/hBN bilayers with different twist angles have been observed in experiments [6,7,9–11] and examined in theoretical studies [8,12,13]. However, most of existing work has focused on a relatively narrow range of small misorientation angles between the two layers, whereas knowledge of higher-angle moiré patterns and the elastic behavior of the bilayers is still sparse, which limits understanding and further development of this type of heterostructural system. This would then require a systematic study of the structural, energetic, and elastic properties of the g/hBN bilayers across a much wider range of interlayer twist angles as will be explored in this paper through efficient multiscale modeling and simulations.

To this end, phase field crystal (PFC) models that were developed and parameterized for the study of 2D layers of graphene [14] and hBN [15] will be exploited. Several different types of PFC models for graphene were examined in Ref. [14] and compared with quantum-mechanical density functional theory (DFT) and molecular dynamics (MD) calculations in terms of energies of grain boundaries, polycrystals, and triple junctions [14,16]. The model termed PFC1 in that work will be used here. In Refs. [15,17] a binary PFC model with sublattice ordering was developed and was used to examine various types of grain boundaries and defect core structures in hBN monolayers with results shown to be in good agreement with experiments and other theoretical studies. These PFC models have been applied and extended to study various other structural and dynamical properties of 2D materials, such as grain rotation and coupled motion in graphene and hBN [18], g/hBN lateral heterostructures [19], ternary 2D hexagonal materials, and in-plane TMD/TMD heterostructures and multijunctions [20]. However, these models

were strictly 2D and did not allow for out-of-plane variations. Recently a simple extension of these models was developed to account for small out-of-plane deformations [21]. Such deformations were shown to significantly lower the energy of dislocations, consistent with other atomistic studies using DFT and MD. In addition, graphene/graphene, graphene/hBN, and hBN/hBN bilayers were also considered there with the coupling between the layers parametrized by fitting to quantum DFT results of stacking energies and heights obtained by Zhou *et al.* [22] with the use of an analytical one-mode approximation for the PFC bilayer models.

In this paper the previous model developed and a more accurate parameter fit to DFT calculations for g/hBN bilayers is used to study inversion domain boundaries of hBN as well as moiré patterns that emerge when the graphene and hBN layers are rotated with respect to each other. The numerical results are not only consistent with previous experimental and theoretical findings, but also provide predictions for the energy density of an inversion boundary in graphene/hBN bilayers and in rotated layers for the twist-angle dependence and a transition of moiré pattern properties and the bilayer elastic state.

In the next sections a description of the model (in Sec. II) and the parametrization through fitting to DFT calculations for the equilibrium states (Sec. III) are presented. This is followed by an examination of inversion domain boundaries in hBN (Sec. IV), showing a reduction of grain boundary energies by 8% to 13.9% as caused by out-of-plane deformations, and a predicted defect configuration of a g/hBN bilayer with an inversion boundary in the hBN layer coupled to a domain wall in the graphene layer. The properties of moiré patterns in twisted g/hBN bilayers are studied in Sec. V as a function of misorientation angle, including the distributions of layer height difference, free-energy density, and volumetric and von Mises (vM) stresses. Of particular focus is the variation in various features of the moiré patterns (e.g., the buckling, energy profile, site occupancy, and stresses) with the bilayer twist angle, revealing a predicted transition to high-angle properties (including smeared-out patterns and stress distribution) that were unknown before. Finally, our conclusions of the results and summary are given in Sec. VI.

II. MODEL

In the PFC model the free-energy functional F for a graphene/hBN bilayer can be written as [21]

$$F = c_{\rm g}(F_{\rm g} + F_{\rm gh}) + c_{\rm h}F_{\rm h}, \tag{1}$$

where $c_{\rm g} = 6.58$ eV and $c_{\rm h} = 2.74$ eV set the energy scales for graphene [14] and hBN [15] layers, respectively. $F_{\rm g}$ is the dimensionless free-energy functional for a flexible graphene layer, i.e.,

$$F_{\rm g} = \int d\vec{r}\Big[\frac{\Delta B}{2}n_{\rm g}^2 + \frac{B^x}{2}\big[(\nabla^2 + q_{\rm g}^2)n_{\rm g}\big]^2 + \frac{\tau}{3}n_{\rm g}^3 + \frac{\upsilon}{4}n_{\rm g}^4 + \frac{\kappa}{2}\int d\vec{r}\,' C_{\rm g}(|\vec{r} - \vec{r}\,'|)h_{\rm g}(\vec{r})h_{\rm g}(\vec{r}\,')\Big], \tag{2}$$

where the Fourier component of $C_{\rm g}$ is given by

$$\hat{C}_{\rm g}(k) = \begin{cases} k^4, & k < k_{\rm max}, \\ C_{\rm max}, & k > k_{\rm max}. \end{cases} \tag{3}$$

In the limit of $\kappa = 0$, Eq. (2) is the model termed PFC1 in Ref. [14]. In Eq. (2), $n_{\rm g}$ is proportional to the atomic number density difference that enters classical density functional theory in the appropriate limit [23], and $h_{\rm g}$ is the height of the graphene sheet. The parameters entering Eq. (2) were fit to graphene in Refs. [14,16,21] and are $\Delta B = -0.15$, $q_{\rm g} = 1$, $B^x = \upsilon = 1$, $\tau = 0.8748$, $\kappa = 0.114$, and the average density $\bar{n}_{\rm g} = 0$. $F_{\rm h}$ is the dimensionless free-energy functional of the hBN layer, given by [15,17]

$$F_{\rm h} = \int d\vec{r}\Big[-\frac{\varepsilon_N}{2}n_{\rm N}^2 + \frac{1}{2}\big[(\nabla^2 + q_{\rm N}^2)n_{\rm N}\big]^2 - \frac{g_{\rm N}}{3}n_{\rm N}^3 + \frac{1}{4}n_{\rm N}^4 - \frac{\varepsilon_{\rm B}}{2}n_{\rm B}^2 + \frac{\beta_{\rm B}}{2}\big[(\nabla^2 + q_{\rm B}^2)n_{\rm B}\big]^2 - \frac{g_{\rm B}}{3}n_{\rm B}^3 + \frac{\upsilon}{4}n_{\rm B}^4 + \alpha_{\rm NB}n_{\rm N}n_{\rm B} + \frac{w}{2}n_{\rm N}^2n_{\rm B} + \frac{u}{2}n_{\rm N}n_{\rm B}^2 + \frac{\kappa_{\rm h}}{2}\int d\vec{r}\,' C_{\rm h}(|\vec{r} - \vec{r}\,'|)h_{\rm h}(\vec{r})h_{\rm h}(\vec{r}\,')\Big], \tag{4}$$

where $n_{\rm N}$ and $n_{\rm B}$ are proportional to the atomic number density differences of the N and B species [17], respectively, and $h_{\rm h}$ is the height of the hBN layer. The parameters have been fitted to hBN [15], with $\varepsilon_{\rm N} = \varepsilon_{\rm B} = 0.3$, $\alpha_{\rm NB} = 0.5$, $g_{\rm N} = g_{\rm B} = 0.5$, $w = u = 0.3$, $\beta_{\rm B} = \upsilon = 1$, and the average densities $\bar{n}_{\rm N} = \bar{n}_{\rm B} = -0.28$. The bending energy coefficient $\kappa_{\rm h}$ was calculated by Guo *et al.* [24] to be 0.89 eV, which in dimensionless units corresponds to 0.32 here. The values of wave-numbers $q_{\rm N}$ and $q_{\rm B}$ are set to a common value $q_{\rm h}$ and will be determined in the next section. $F_{\rm gh}$ is the dimensionless free-energy functional representing the coupling between the two layers, given by

$$F_{\rm gh} = a_2\int d\vec{r}\,(\Delta h - \Delta h^0)^2 + \int d\vec{r}(V_{\rm N}n_{\rm N} + V_{\rm B}n_{\rm B})n_{\rm g}, \tag{5}$$

where $\Delta h = h_{\rm g} - h_{\rm h}$ and

$$\Delta h^0 = \Delta[1 + n_{\rm g}(\alpha_{\rm gN}n_{\rm N} + \alpha_{\rm gB}n_{\rm B})]. \tag{6}$$

This form is similar to that reported by Elder *et al.* [21], but for computational efficiency, the coupling is among $n_{\rm N}$, $n_{\rm B}$, and $n_{\rm g}$ and not among the differences from the average densities (i.e., $n_{\rm N} - \bar{n}_{\rm N}$ etc.) which were simpler for analytic calculations. The parameters entering Eqs. (5) and (6) (i.e., a_2, Δ, $\alpha_{\rm gN}$, $\alpha_{\rm gB}$, $V_{\rm N}$, and $V_{\rm B}$) will be discussed in more detail in the next section. Finally to allow for out-of-plane deformations the Laplacian entering Eqs. (2) and (4) becomes

$$\nabla^2 \to \big(1 - h_x^2\big)\partial_{xx} + \big(1 - h_y^2\big)\partial_{yy} - 2h_xh_y\partial_{xy}, \tag{7}$$

where $h_i \equiv \partial_i h$ and the h field entering Eq. (7) is $h_{\rm g}$ in Eq. (2) and $h_{\rm h}$ in Eq. (4).

As discussed in Refs. [14,15], Eqs. (2) and (4) are in essence the original PFC model (with some couplings between two components in the hBN case) that are minimized by a periodic structure due to the term $(\nabla^2 + q_X^2)$, where X is g, B or N and q_X uniquely determines the lattice periodicity for a given set of parameters. The other polynomial terms in the free-energy functional are essentially a standard Landau

expansion that gives rise to two potential wells of differing height, which breaks the up-down symmetry and leads to 2D triangular patterns as opposed to one-dimensional stripe patterns. The corresponding coefficients can be connected to the Fourier components of the expansion of direct correlation functions in classical DFT [15,17,23]. For convenience q_g was set to unity and as discussed in the next section, q_B and q_N were chosen to give the correct graphene/hBN lattice constant ratio. Details of the choice of the parameters entering Eqs. (2) and (4) are given in Refs. [14,15], respectively. Details of the graphene-hBN layer coupling [i.e., Eq. (5)] are discussed in Ref. [21] as well as in the following section.

The dynamics of the fields are conserved for the densities and nonconserved for the heights, i.e.,

$$\frac{\partial n_\alpha}{\partial t} = \nabla^2 \frac{\delta F}{\delta n_\alpha}, \tag{8}$$

and

$$\frac{\partial h_\alpha}{\partial t} = -\Gamma \frac{\delta F}{\delta h_\alpha}, \tag{9}$$

where the subscript $\alpha = \mathrm{g}, \mathrm{h}$ corresponds to either graphene (g) or hBN (h). Since the focus of this paper is on equilibrium states, Γ was chosen as large as possible to get to equilibrium. Typically, $\Gamma \approx 10$–50, although in some cases after initial relaxation it was possible to increase Γ up to 10 000. In all the following calculations periodic boundary conditions are used.

III. EQUILIBRIUM

For simplicity the wave-numbers q_N and q_B will be set identical, i.e., $q_N = q_B = q_h$ in the hBN layer. In the lowest-order Fourier expansion of the density fields q_h is given by

$$q_h = a_g/a_h, \tag{10}$$

where a_g and a_h are the lattice constants of the graphene and hBN layers, respectively. However, as will be discussed below, q_h must be numerically fitted since higher-order Fourier modes will play a non-negligible role in determining the lattice constants. It is useful to rewrite the dimensionless bilayer free-energy functional F as

$$\frac{F}{c_g} = F_g + F_{gh} + \frac{c_h}{c_g} F_h, \tag{11}$$

to incorporate the ratio c_h/c_g in numerical simulations. It was found that if q_h were set to

$$q_h = 1.011 a_g/a_h, \tag{12}$$

the dimensionless lattice constants obtained numerically became

$$a_h = 7.4191, \qquad a_g = 7.2721. \tag{13}$$

This then gives $a_g/a_h = 0.9802$, which is close to the ratio $2.46/2.51 = 0.9801$ between graphene (of lattice constant 2.46 Å) and hBN (2.51 Å).

To ascertain the nature of the equilibrium state, a bilayer was constructed with 49×49 unit cells of hBN and 50×50 of graphene. This turned out to be an unstable initial condition which spontaneously relaxed to the graphene layer becoming commensurate (49×49 unit cells) with the hBN layer. Next the free-energy density of a commensurate g/hBN bilayer system was examined as a function of the lattice constant a_b^x of the bilayer. It was found that the lowest-energy state occurred when

$$a_b^x = 7.3548, \tag{14}$$

or 2.488 Å in dimensional units and is slightly closer to the hBN lattice constant, i.e., $a_b^x - a_g = 0.083$ and $a_h - a_b^x = 0.064$.

The free-energy density difference $\Delta F/A$ (with area A) and the relative height Δh^{eq} were examined for the bilayer as a function of stacking position, where ΔF is the difference with respect to the AB stacking. The stacking is illustrated in Fig. 1, for densities $n_g(x, y + y_0)$ and $n_{B(N)}(x, y)$ such that when $y_0 = 0$ an AB stacking (the lowest-energy state) occurs. The parameters as listed in Table I were initially chosen using the analytic one-mode approximation (which includes only the lowest-order Fourier coefficients needed to reconstruct the graphene and hBN crystalline lattices) as described by Elder *et al.* [21]. They were obtained by fitting to the DFT calculations of Zhou *et al.* [22] which considered four different DFT approaches and determined the one with adiabatic-connection fluctuation-dissipation theorem within the random phase approximation (ACFDT-RPA) giving the best predictions for bulk properties; as such these data were used to fit the current PFC model. Their predictions for $\Delta F/A$ and equilibrium Δh^{eq} are shown in Figs. 2 and 3, respectively. Numerical simu-

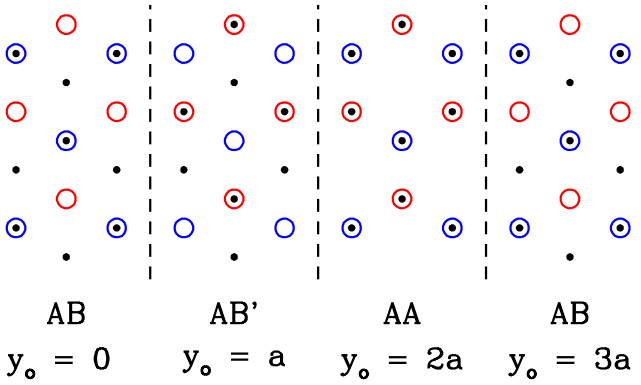

FIG. 1. Stacking for the graphene/hBN bilayer. The black, blue and red points correspond to density maxima in n_g, n_N, and n_B, respectively. y_0 is the shift of the graphene lattice with respect to the hBN lattice, and a is the nearest-neighbor distance.

TABLE I. Summary of model parameters for the graphene/hBN bilayer PFC model.

Model parameter	One-mode approximation	Adjusted value
V_N	2.06×10^{-4}	2.25×10^{-4}
V_B	2.64×10^{-5}	5.20×10^{-5}
Δ	10.31	10.32
α_{gN}	0.195	0.21
α_{gB}	0.037	0.07
a_2	7.31×10^{-5}	7.31×10^{-5}

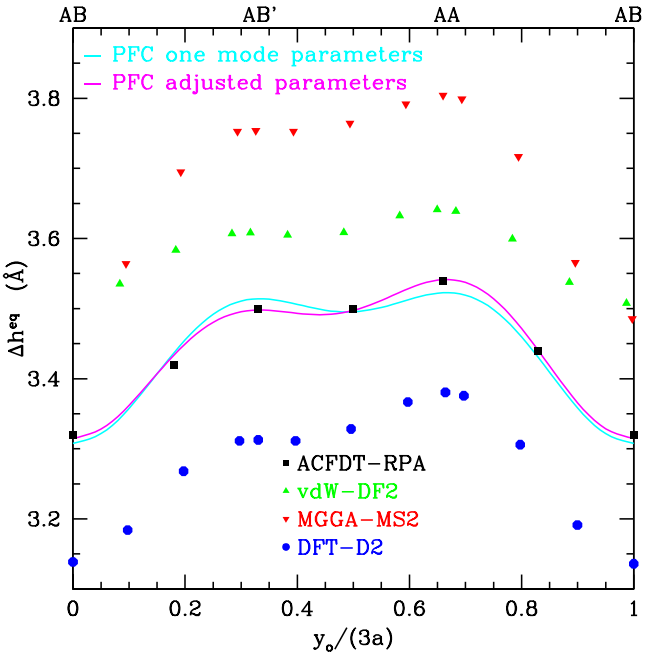

FIG. 2. Stacking height predictions. The DFT calculations [adiabatic-connection fluctuation-dissipation theorem within the random phase approximation (ACFDT-RPA), van der Waals density functionals (vdW-DF2), meta–generalized gradient approximation (MGGA-MS2), and Grimme's density functional dispersion correction (DFT-D2)] are from Zhou *et al.* [22].

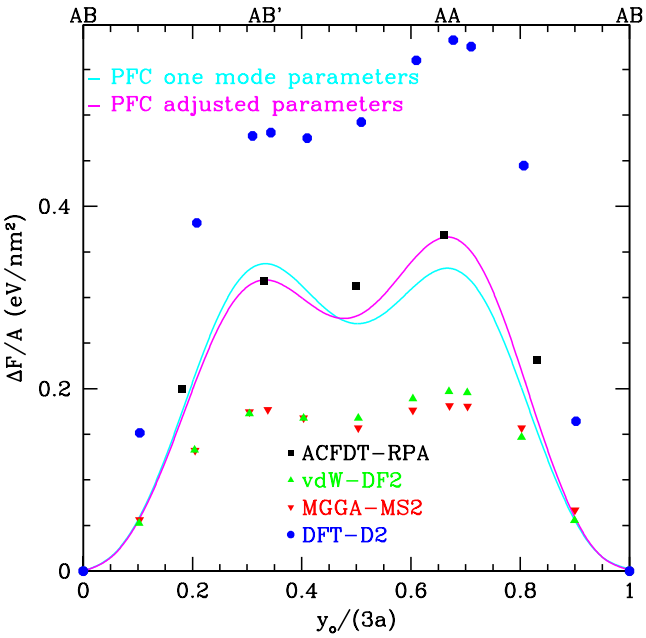

FIG. 3. Stacking energy-density predictions. The DFT calculations (ACFDT-RPA, vdW-DF2, MGGA-MS2, and DFT-D2) are from Zhou *et al.* [22].

lations of the PFC model were conducted (which naturally include all Fourier coefficients) to minimize the free energy for an AB stacking. This configuration was then used to determine the energy of other stackings as described by Elder *et al.* [21]. As with the DFT calculations these were performed on a single unit cell which does not allow for out-of-plane deformations. The outcomes of these studies show that results from the one-mode parameters are close to the DFT calculations but are slightly different with small deviations for the height and free-energy density difference between the AB′ and AA stackings as seen in Figs. 2 and 3. One particular feature is that in the one-mode predictions the magnitude of Δh^{eq} and $\Delta F/A$ are very similar for the AB′ and AA stackings which, however, are clearly different in all the DFT calculations. For this reason the parameters were adjusted to obtain a better fit as shown in both Figs. 2 and 3. A summary of the corresponding dimensionless parameters obtained are given in Table I. These adjusted parameters are used in all the subsequent simulations that follow.

IV. INVERSION DOMAIN BOUNDARIES IN HBN AND THE GRAPHENE/hBN BILAYER

In a prior publication [15] an examination of inversion boundaries in hBN was performed using a rigid model, i.e., using the free-energy functional in Eq. (4) with $h_{\mathrm{h}} = 0$. An inversion boundary forms when the atomic ordering switches from BNBNBN to NBNBNB as illustrated in Fig. 4. As drawn in the figure the boundary contains many homoelemental nearest neighbors in the middle portion, which would be very unfavorable energetically. Instead the system prefers to form defected structures with unit rings that contain more or less than six atoms but avoid having homoelemental B-B or N-N

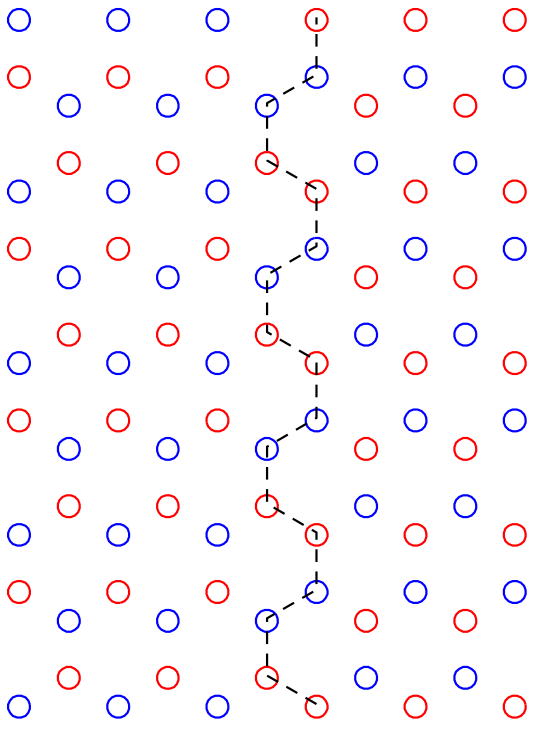

FIG. 4. Illustration of an unstable inversion domain boundary. The blue and red dots indicate N and B atoms, respectively, and the dashed black line highlights the inversion boundary.

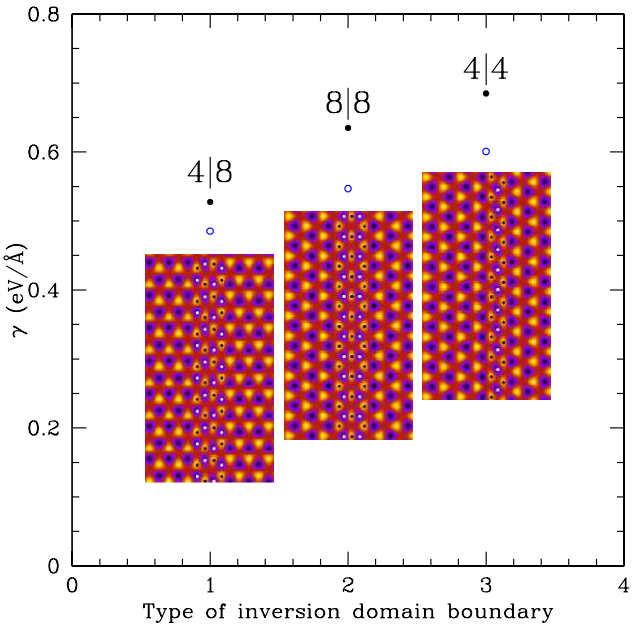

FIG. 5. Inversion boundary energy γ of three lowest-energy inversion domain boundaries in hBN monolayers. The solid black and open blue dots above the snapshots correspond to rigid and flexible sheets, respectively, where the energy was minimized with respect to the dimensions of the simulation box. Note that only one unit cell was included in the y direction. In the configurations, blue and yellow maxima correspond to the positions of the N and B atoms, respectively, and black and white dots have been placed on lattice locations at the inversion boundaries.

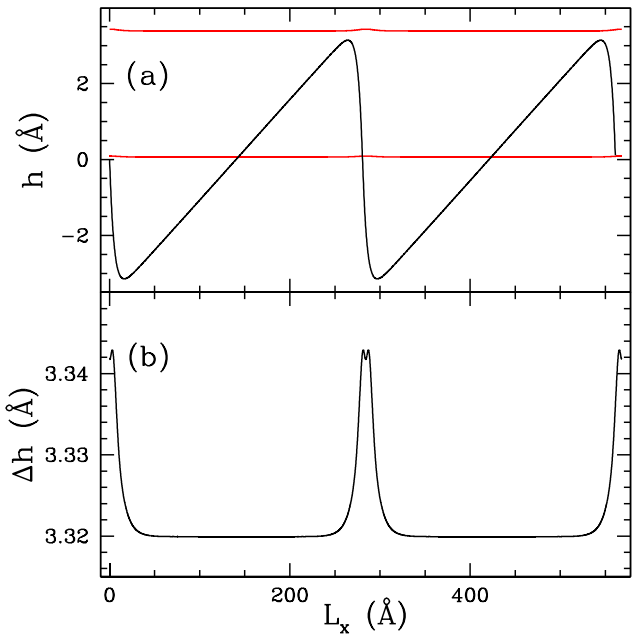

FIG. 6. (a) Comparison of height variation across two 4|8 inversion boundaries in a single monolayer of hBN (black curve) and a g/hBN bilayer (red lines), where the upper (lower) red line is for graphene (hBN) in the bilayer. (b) Height difference between the graphene and hBN layers in the g/hBN bilayer [i.e., the difference between the red lines in (a)].

neighboring. In particular, the grain boundary energy per unit length (γ) of inversion boundaries that contain 4|8, 8|8, and 4|4 defect structures will be studied, where $i|j$ corresponds to neighboring defect pairs containing i- and j-membered atomic rings. In prior work [15] it was found that the 4|8 boundary naturally emerges when the boundary is along the armchair (AC) direction, whereas the 8|8 results from the zigzag (ZZ) orientation. There was also a 4|4 boundary along a ZZ interface that was slightly shifted; hence, strictly speaking the 4|4 is not an inversion boundary due to the shift (see Fig. 5).

In this section inversion boundaries will be examined for a flexible hBN monolayer and a hBN/graphene bilayer. These studies will illustrate the impact of allowing out-of-plane deformations on a single layer as well as the influence of the hBN inversion boundary on the graphene layer in a bilayer system.

Simulations were first conducted to reproduce the results of Taha *et al.* [15]. A fully periodic box of size $L_x\Delta x \times L_y\Delta y$, where L_x and L_y are integers, was used. In these simulations a box of grid size $3200\Delta x \times 24\Delta y$ for the AC configuration and $3200\Delta x \times 14\Delta y$ for the ZZ configuration were used. This corresponds to boxes of size 563×4.22 Å^2 for the AC and 563×2.46 Å^2 for ZZ, and corresponds to a single unit cell in the x direction. It should be noted that conserved dynamics [i.e., Eq. (8)] were employed, which do not fix the local density whereas ensuring a constant average density in the whole system. Taha *et al.* [15] typically found grain boundary energies saturate for system sizes of 500 Å and larger. For the rigid case (without out-of-plane deformations) the initial condition was such that half the simulation box was of configuration NBNB whereas the other half was BNBN with a uniform density band of width $20\Delta x$ placed at the boundaries. Simulations were run until the system energy was minimized. Next, Δx and Δy were varied to find the minimum energy state (since it is not possible to know the desired width of the domain walls). In the simulations here (flexible hBN monolayer and hBN/graphene bilayer) the same procedure was followed. Fixing $h = 0$ reproduced the results of Taha *et al.* [15] for the 2D rigid planar systems.

Following these simulations were conducted for a flexible sheet allowing out-of-plane deformations (i.e., containing variations in h). A first test was conducted on a system of size 563×169 Å^2 with the initial condition set up by reproducing 40 lattice constants for an AC boundary along the x direction. The initial height was set to be a uniform random number in the range of $-1/8 < h < 1/8$. The simulation results showed that the height developed into a one-dimensional pattern perpendicular to the domain wall [see Fig. 6(a)]. This indicates that one unit cell along the parallel direction of this pattern was sufficient. Allowing for out-of-plane deformations lowered the domain-wall energy as shown in Fig. 5. Despite a modest bending of the sheet [on the order of one atomic spacing, as seen in, e.g., Fig. 6(a)], a considerable decrease in system energy was observed (by 8.0%, 13.9%, and 9.4%, respectively, for 4|8, 8|8, and 4|4 boundaries).

A further simulation was conducted to understand the influence of such boundaries in g/hBN bilayers. The initial

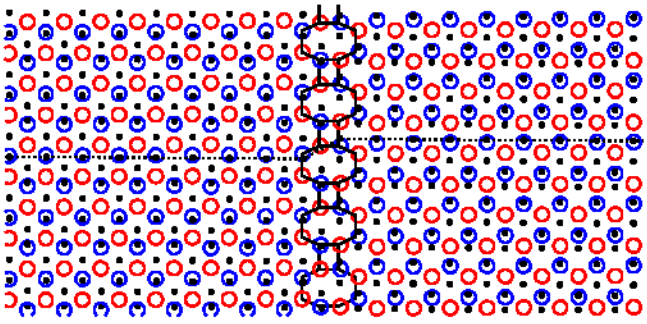

FIG. 7. Structure of inversion boundary in a g/hBN bilayer obtained from numerical simulations. The color/point scheme is the same as that in Fig. 1. The dashed line is a guide to the eye to highlight the domain wall in the graphene lattice across the inversion boundary. Note that only one unit cell is simulated in the y direction.

condition for the hBN layer was the same as that described for the monolayer case except the lattice constant used (2.488 Å) was the one that minimizes the g/hBN bilayer as discussed in Sec. III. The graphene layer was initialized to be in an AB stacking configuration on both sides of the grain boundary. Near the boundaries the graphene density was set to be uniform in a width of $20\Delta x$ so that a boundary would naturally form. This leads to an inversion boundary in the hBN layer with 4|8 defect pairs and a domain wall in the graphene layer in which the graphene slides perpendicular to boundary as illustrated in Fig. 7. As can be seen in this figure the graphene layer remains in the AB stacking but the atomic sites need to shift across the boundary, leading to in-plane local distortions and strain in the graphene layer. Initially the heights in both layers resemble that of the monolayer case; however, as time evolves larger height gradients appeared at the boundaries, leading to numerical instabilities. In order to eliminate the instability the grid spacings in both the x and the y directions were reduced by a factor of 2. With this change during the time evolution the heights spontaneously transformed into a much smoother profile eventually as shown in Figs. 6(a) and 6(b).

The free-energy difference per unit length was measured to be $\gamma = 0.471$ eV/Å for the inversion boundary in the g/hBN bilayer system. Although it is somewhat interesting that this value is comparable to the single-layer result of hBN, it is important to note that in the single-layer system the inversion boundary energy was compared to an unstrained, flat equilibrium hBN layer (with lattice constant $a_h = 2.51$ Å), whereas for the bilayer it was compared to a configuration with lattice constant 2.488 Å that minimizes the bilayer where both the graphene and the hBN layers are strained in the lowest-energy state. This significantly restricts out-of-plane deformations since the hBN layer is under compression and graphene under tension. In addition, the bilayer is a three-dimensional system. The three-dimensional inversion boundary energy γ_{3d} is $0.471/3.32 = 0.142$ eV/Å^2, where 3.32 Å is the vertical spacing between the layers.

Although these simulations give insights of the influence of a defect (i.e., inversion boundary in hBN) in the coupled layers, it should be noted that the quantitative results will depend on the specific setup. In the above simulations an inversion boundary was formed in hBN at the equilibrium lattice constant (2.488 Å) of the g/hBN bilayer system. This would be quantitatively different from growing graphene on an already formed hBN inversion boundary that was at the lattice constant (2.51 Å) of a single hBN layer. In addition, the procedure in the simulations conducted here was to adjust the width and length of the system to minimize the free energy. Presumably changes in the setup and procedure could lead to quantitatively different results, although they are unlikely to change the qualitative structures in the two layers, such as the domain walland its resulting strain in the graphene layer.

V. TWISTED BILAYERS

To study a twisted bilayer of graphene and hBN numerically, one layer was rotated by angle θ and the other by $-\theta$, for a total misorientation of 2θ with both lattice constants set to those identified in Sec. III, i.e., 2.48 Å. This gives rise to the appearance of moiré patterns and some interesting behavior as observed in many previous works [21,22,25,26]. As discussed in Ref. [21] only certain rotation angles and box sizes can be used in a periodic simulation box. More precisely, given an integer k in the zigzag orientation with rotation angle,

$$\tan\,\theta = \frac{\sqrt{3}}{2(k+1/2)}, \tag{15}$$

the system size (L_x, L_y) must be

$$L_x = a_x\sqrt{3/4 + (k+1/2)^2}, \qquad L_y = \sqrt{3}L_x, \tag{16}$$

where $a_x = 4\pi/(\sqrt{3}\,q_{\min})$. A typical configuration at a small angle is presented in Fig. 8. The wavelength λ of the moiré pattern shown in this figure is given by $\lambda = L_x/\sqrt{3}$. The figure indicates that the height difference is the smallest in the AB

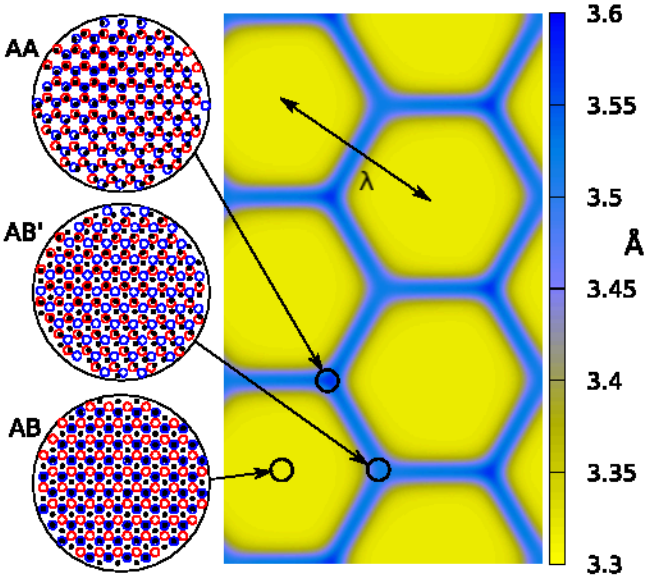

FIG. 8. Sample configuration for misorientation $2\theta = 0.66°$ (for $k = 150$) and pattern wavelength $\lambda = 21.4$ nm. The color scheme on the right corresponds to the height difference between the layers. The size of the configuration is 37.0×64.1 nm^2. On the left the atomic configurations are shown for the circled regions. The color scheme is the same as that of Fig. 1.

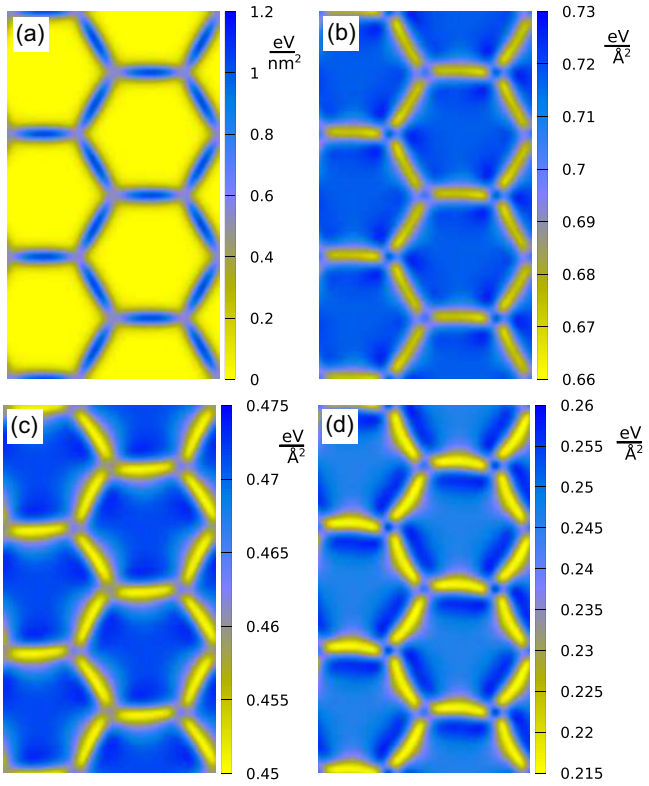

FIG. 9. Sample configurations at misorientation $2\theta = 0.66^\circ$ for (a) smoothed free-energy density difference and the smoothed volumetric stress in (b) the combined bilayer, (c) graphene, and (d) hBN layers, respectively. The scale is in units of eV/nm^2 in (a) and eV/Å^2 in (b)–(d). The size of the system is the same as that of Fig. 8.

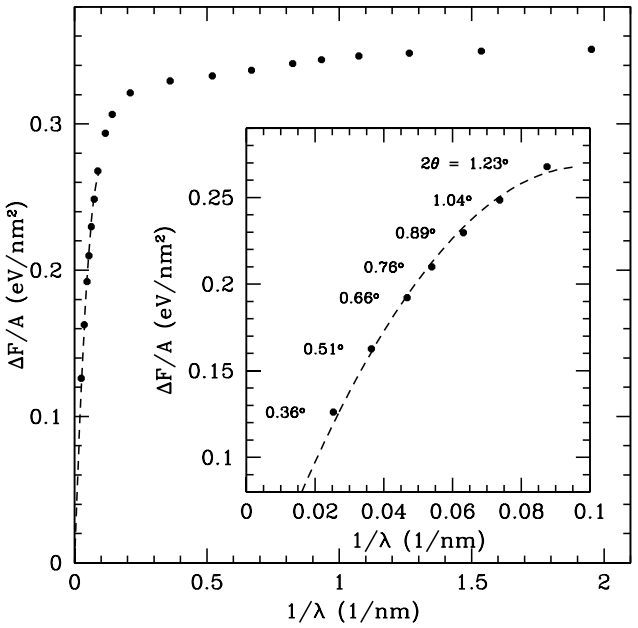

FIG. 10. Free-energy density difference as a function of $1/\lambda$. The points correspond to simulation data, and the dashed line corresponds to a second-order polynomial fit to $\Delta F/A$ in terms of $1/\lambda$ according to Eq. (17) for $1/\lambda < 0.10$ nm^{-1}.

stacking regions and the largest at the AA junctions, followed by the AB′ junctions, consistent with Fig. 2. This makes the pattern slightly nonsymmetric or tilted.

Sample configurations are shown in Fig. 9 for the corresponding free-energy density and the volumetric stress, $\sigma_V = \sigma_{xx} + \sigma_{yy}$ of the whole system and individual layers. These quantities vary on the length scale of the atomic spacing, which makes it difficult to observe the overall pattern. For this reason in the visualization of patterns they were smoothed via the multiplication of $e^{-\alpha_0 k^2}$ in Fourier space, where k is the wave number, and then an inverse Fourier transform. A value of $\alpha_0 = 14$ was found to mostly eliminate the small scale oscillations whereas not washing out the large-scale moiré patterns and was used for the pattern visualization of all angles. Figure 9 shows that the triple junctions in the pattern are slightly twisted, particularly, evident in the σ_V spatial distribution of individual layers [see panels (c) and (d)] from which it is also interesting to note that the junctions in two layers twist in opposite directions. Similar twisted junctions have been observed in many other strained-layer moiré patterns [25,27–32]. This twisting occurs to move the junctions to lower the junction energy, even though this slightly increases the length of the domain walls connecting the junctions.

For very small angles it is possible to postulate that the system free energy would scale as $F = 2\chi + (3\lambda/\sqrt{3})\gamma + Af_c$, where χ is the free energy of the junction, γ is the energy per unit length of the domain wall, f_c is the free-energy density of the commensurate regions, and $A = (\sqrt{3}/2)\lambda^2$ is the area of a hexagon in the pattern. The factor of 2 in front of χ is due to the fact that each junction contributes $\chi/3$ to each hexagon, and there are six junctions per hexagon. The $3\lambda/\sqrt{3}$ factor in front of γ arises from the fact that each domain-wall length

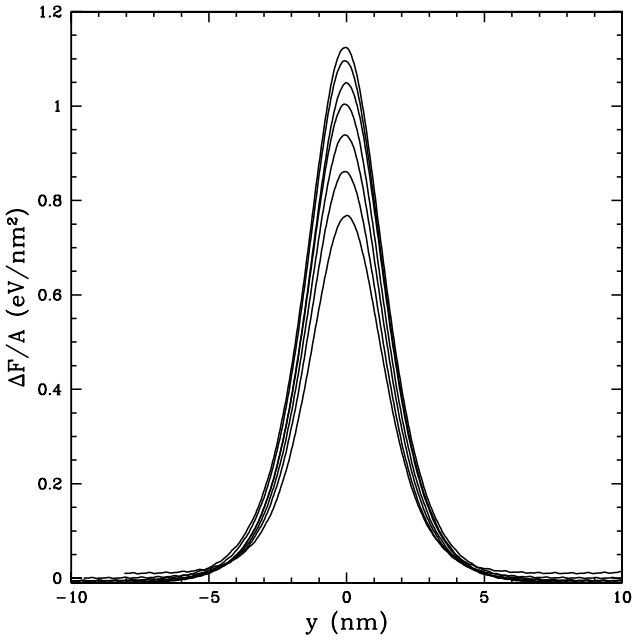

FIG. 11. Free-energy density difference across a domain wall. The lines from top to bottom correspond to angles $2\theta = 0.36^\circ$, 0.51°, 0.66°, 0.76°, 0.89°, 1.04°, and 1.23°.

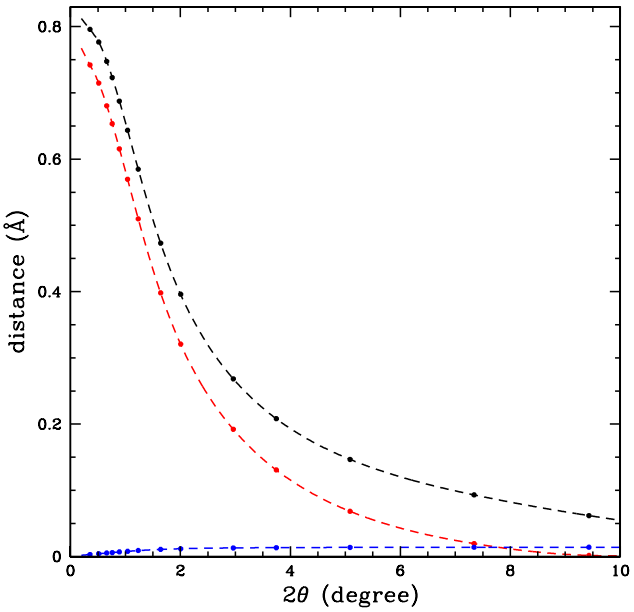

FIG. 12. Buckling of the hBN (black line) and graphene (red line) layers as a function of misorientation. In addition, the difference of the average distance between layers with respect to the equilibrium AB-stacking distance (i.e., $\langle h_h - h_g \rangle - \Delta h_{AB}$) is shown in blue. The lines are guides to the eye.

is $\lambda/\sqrt{3}$ and that there are six domain walls per hexagon with each wall contributing to two hexagons. This then implies that the free-energy density difference scales as

$$\frac{\Delta F}{A} = \frac{4}{\sqrt{3}}\frac{\chi}{\lambda^2} + \frac{2\gamma}{\lambda}. \tag{17}$$

The total free-energy density of the bilayer is shown as a function of the inverse periodicity $(1/\lambda)$ of the pattern in Fig. 10, which includes a fit to the form $\Delta F/A = \alpha/\lambda + \beta/\lambda^2$ for the small angle data. This gives a prediction for the junction energy $\chi = -11.9$ eV and domain-wall energy density $\gamma = 2.71$ eV/nm. These results should be taken with a grain of salt as they assume λ is much larger than the size of the defects (domain walls and junctions) and that the specific form of defects does not change with system size. However, it is clear that there are, in fact, changes in these defects as shown in Fig. 11, where the free-energy density across a domain wall can be seen to increase with larger system size.

The change in free-energy density is also accompanied by a change in the buckling of the individual layers. In Fig. 12 the buckling width $\sqrt{\langle (h_\alpha - \bar{h}_\alpha)^2 \rangle}$ (where α refers to the g or hBN layer) is depicted. The buckling reaches a maximum as $\theta \to 0$ and becomes very small for large angles as has been observed in other studies [33]. Also shown in this figure is the average distance between the layers minus the equilibrium AB-stacking distance. As can be seen this distance is much smaller than the buckling of the individual layers, indicating

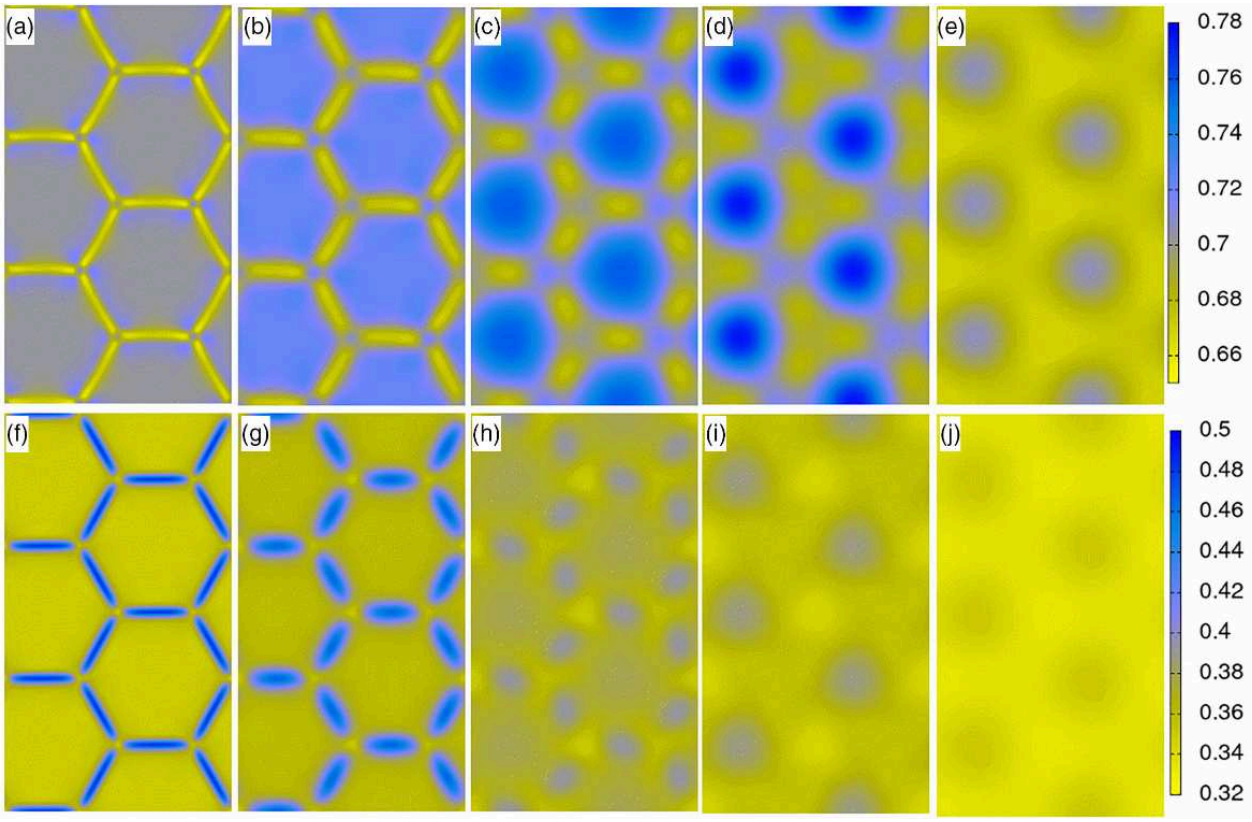

FIG. 13. Smoothed volumetric [(a)–(e)] and von Mises [(f)–(j)] stresses for misorientation angles and pattern wavelengths $(2\theta, \lambda) =$ (0.36°, 39.6 nm), (0.76°, 18.5 nm), (1.64°, 8.5 nm), (2.96°, 4.8 nm), and (9.43°, 1.5 nm) for (a)–(e) or (f)–(j), respectively. The color scale is in units of eV/nm^2. In each instance the system size is $\sqrt{3}\lambda \times 3\lambda$.

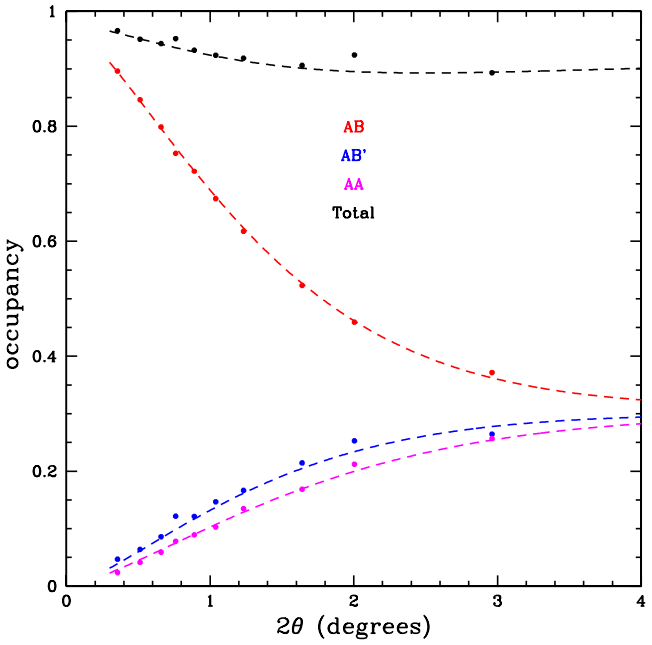

FIG. 14. Occupancy of AA, AB′, and AB sites as a function of misorientation. The black points correspond to the sum of the AB, AB′, and AA occupancies. The lines are guides to the eye.

that the sheets buckle in sync with each other as has been observed in graphene/graphene bilayers [21,22,30].

More interesting than the buckling is the change in stress as a function of misorientation. The picture of well-defined domain walls and junctions breaks down for large misorientations when the domain walls become comparable with the size of the moiré pattern. This can be well captured by the

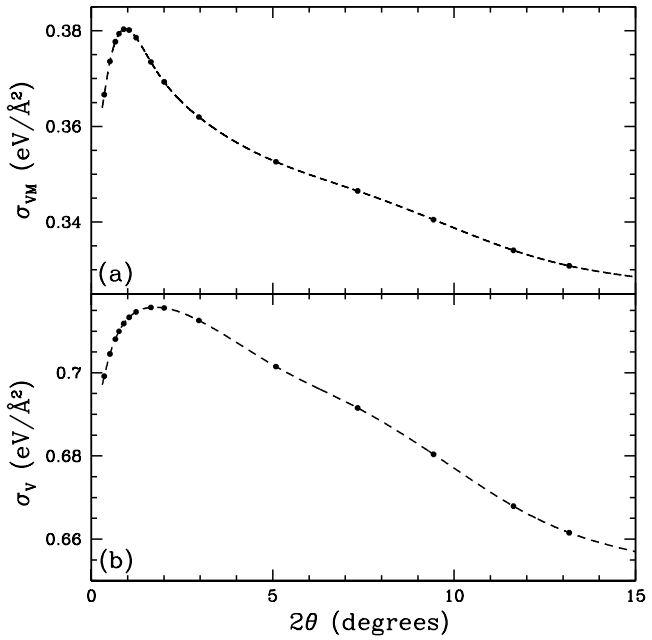

FIG. 15. Average von Mises and volumetric stresses as a function of misorientation in (a) and (b), respectively.

volumetric (σ_V) and von Mises [34] (σ_{VM}) stresses, where the latter is given by $\sigma_{VM} = \sqrt{\sigma_{xx}^2 + \sigma_{yy}^2 - \sigma_{xx}\sigma_{yy} + 3\sigma_{xy}^2}$ in 2D after neglecting the z-direction stress components. The corresponding results are shown in Fig. 13. The patterns exhibit a transition from those with well-defined triple junctions and domain walls to smeared-out patterns around $\theta \approx 0.5^\circ - 0.8^\circ$ (with $\lambda = 15$–25 nm). As can be seen in Fig. 11 the size of the domain wall is on the order of 5–10 nm; thus, the transition occurs roughly when the domain walls begin to overlap. In this case there are no well-defined AB, AB′, and AA regions as indicated in Fig. 14, which shows the occupancy of these states as a function of θ. It should be noted that it was not always possible to determine the state of a given unit cell; i.e., as shown in this figure the sum of the occupancy does not add to one. Clearly for small angles the AB states dominate since they are the lowest-energy phases, followed by the next lowest-energy state AB′ and finally by the AA state as expected. This also implies that for small angles the AA junctions are slightly smaller than the AB′ junctions.

The transition from small- to large-angle patterns can be identified from the average von Mises and volumetric stresses as given in Fig. 15. Both become larger with the increase in misorientation angle, then reach a peak before slowly decreasing. The peak in σ_{VM} occurs at $2\theta = 1.03^\circ$ and in σ_V appears at $2\theta = 1.76^\circ$, consistent with the observation in spatial profiles of stress distribution in Fig. 13 which show the transition between two different types of moiré patterns. However, it is interesting to note the differences between the patterns. In the volumetric case the stress is largest in the commensurate regions and smallest at the domain walls. This is the exact opposite of the von Mises stress, which is most apparent at small misorientations as seen in Fig. 13. The spatial difference between the two stresses is likely due to the fact that von Mises stress incorporates effects of distortion and shearing, and, thus, would be large at domain walls, while volumetric (hydrostatic) stress accounts for the effect of volume change but not distortion or shear, and, thus, would be small at domain boundaries but large in the domain bulk subjected to lattice compression or tension. In addition, in the volumetric case the stress increases in the commensurate regions with increasing angle until the transition to the smeared-out state occurs. In contrast, the von Mises stress in the commensurate regions does not vary as much with the change of misorientation. It appears that as the angle decreases from large values, domain walls emerge, which increases the von Mises stress until the walls are fully formed. When the angle is further reduced, the total von Mises stress decreases as the relative area of the domain wall compared to well-separated commensurate region becomes smaller. This results in a maximum of average stress around a transition angle as shown in Fig. 15. This change in von Mises stress distribution indicates the change in mechanical property (e.g., yielding) of the bilayer across the transition of the moiré pattern.

As a final note it is interesting to contrast these results with the moiré patterns that appear in graphene/graphene bilayers. The main difference is that in a graphene/graphene bilayer the AB′ stacking would have an energy identical to the AB stacking, i.e., in such a bilayer no AB′ junction would exist. This completely changes the symmetry of the domain wall

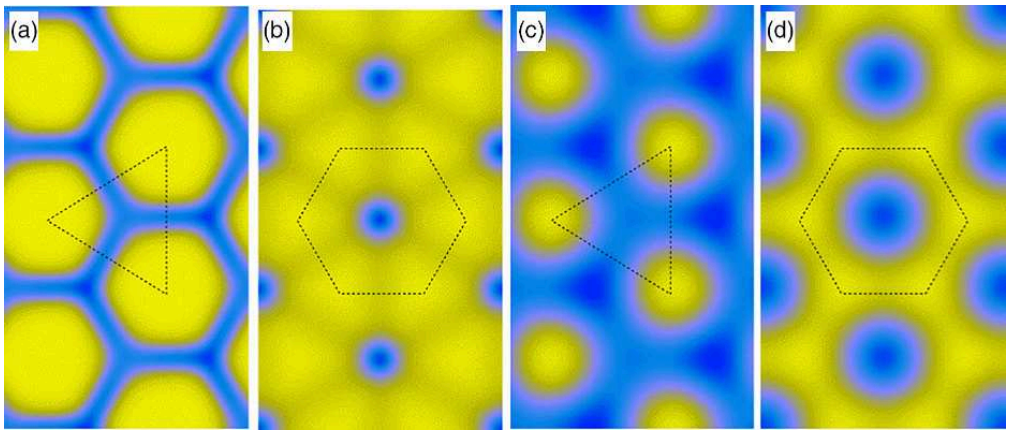

FIG. 16. Comparison of height differences at misorientations $2\theta = 1.04^\circ$ in (a) and (b) and $2\theta = 3.74^\circ$ in (c) and (d). (a) and (c) correspond to the graphene/hBN bilayer and (b) and (d) to the graphene/graphene bilayer. The dotted black line is a guide to the eye to illustrate the triangular and hexagonal ordering of the commensurate regions in the graphene/hBN and graphene/graphene bilayers, respectively. In (a) and (c) the scale varies from 3.25 Å (yellow/light) to 3.6 Å (blue/dark) and in (b) and (d) from 3.25 to 3.55 Å. The system sizes are (a) 23.5 × 40.7 nm^2, (b) 23.2 × 40.2 nm^2, (c) 6.5 × 11.3 nm^2, and (d) 6.4 × 11.2 nm^2.

and defect structures from triangular in graphene/graphene bilayers to a honeycomb shape in g/hBN bilayers. A comparison of the two different systems is shown in Fig. 16 for two different misorientations. The commensurate regions (with lowest height differences, appearing yellow/light in the figure) of these two types of bilayers have inverse symmetry with respect to each other, i.e., a triangular pattern forms in the g/hBN bilayer and honeycomb in the graphene/graphene bilayer.

VI. SUMMARY AND CONCLUSIONS

In this paper a 2D PFC model incorporating out-of-plane deformations was examined for hBN and graphene/hBN bilayers. In the bilayer case, the model was parametrized numerically to closely match the ACFCT-RPA DFT calculations for stacking energies and height differences between the graphene and the hBN layers obtained by Zhou *et al.* [22], which improves the previous analytic one-mode calculations of Ref. [21]. It was shown that out-of-plane deformations lead to significantly lower inversion boundary energies in hBN on the order of ≈8%–14%. The boundary in the g/hBN system results in the formation of a domain wallwith local distortions in the graphene lattice. This interesting defect configuration in the g/hBN bilayer gives a domain-wall energy of $\gamma_{3d} = 0.142$ eV/Å^2 as predicted from this PFC calculation.

Numerical simulations were conducted to examine the moiré patterns that form when the bilayers are rotated with respect to each other, showing regions of different types of stacking positions between the layers. For small rotations the patterns consisted of well-defined hexagon-shaped domain walls with triple junctions twisting in opposite directions in graphene versus hBN layers. Results of the system free-energy density, layer height difference, buckling, and smoothed volumetric and von Mises stresses have been obtained for a range of bilayer misorientation angles (and moiré pattern wavelengths) that go beyond previous studies. An interesting phenomenon observed is the breakdown of well-distinguished domain-wall structures in the moiré pattern at large enough misorientation when the domain-wall width and the pattern size are of compatible scale, leading to the transition to a different type of smeared-out moiré pattern with overlapping domain boundaries. The corresponding elastic variations of these bilayer systems, in terms of volumetric and von Mises stresses, have been identified, serving as a useful way to characterize the moiré pattern, transition, and the mechanical property of this type of vertical heterostructures.

ACKNOWLEDGMENTS

K.R.E. acknowledges support from the National Science Foundation (NSF) under Grant No. DMR-2006456 and Oakland University Technology Services high performance computing facility (Matilda). Z.-F.H. acknowledges support from NSF under Grant No. DMR-2006446. T.A-N. has been supported, in part, by the Academy of Finland through its QTF Center of Excellence program Grant No. 312298. K.R.E. also acknowledges useful discussions with M. Greb.

[1] D. Akinwande, C. Huyghebaert, C.-H. Wang, M. I. Serna, S. Goossens, L.-J. Li, H.-S. P. Wong, and F. H. L. Koppens, Nature (London) **573**, 507 (2019).

[2] P. Ajayan, P. Kim, and K. Banerjee, Phys. Today **69**(9), 38 (2016).

[3] F. Guinea and N. R. Walet, Proc. Natl. Acad. Sci. USA **115**, 13174 (2018).

[4] M. Yankowitz, S. Chen, H. Polshyn, Y. Zhang, K. Watanabe, T. Taniguchi, D. Graf, A. F. Young, and C. R. Dean, Science **363**, 1059 (2019).

[5] F. Momeni, B. Mehrafrooz, A. Montazeri, and A. Rajabpour, Int. J. Heat Mass Transf. **150**, 119282 (2020).
[6] C. R. Dean, L. Wang, P. Maher, C. Forsythe, F. Ghahari, Y. Gao, J. Katoch, M. Ishigami, P. Moon, M. Koshino *et al.*, Nature (London) **497**, 598 (2013).
[7] B. Hunt, J. D. Sanchez-Yamagishi, A. F. Young, M. Yankowitz, B. J. LeRoy, K. Watanabe, T. Taniguchi, P. Moon, M. Koshino, P. Jarillo-Herrero *et al.*, Science **340**, 1427 (2013).
[8] P. Moon and M. Koshino, Phys. Rev. B **90**, 155406 (2014).
[9] T. Iwasaki, S. Nakaharai, Y. Wakayama, K. Watanabe, T. Taniguchi, Y. Morita, and S. Moriyama, Nano Lett. **20**, 2551 (2020).
[10] S. Tang, H. Wang, Y. Zhang, L. Ang, H. Xie, X. Liu, L. Liu, T. Li, F. Huang, X. Xie *et al.*, Sci. Rep. **3**, 2666 (2013).
[11] X. Huang, L. Chen, S. Tang, C. Jiang, H. Wang, Z.-X. Shen, H. Wang, and Y.-T. Cui, Nano Lett. **21**, 4292 (2021).
[12] C. Hu, V. Michaud-Rioux, X. Kong, and H. Guo, Phys. Rev. Mater. **1**, 061003(R) (2017).
[13] Y. Chandra, E. I. Saavedra Flores, and S. Adhikari, Comput. Mater. Sci. **177**, 109507 (2020).
[14] P. Hirvonen, M. M. Ervasti, Z. Fan, M. Jalalvand, M. Seymour, S. Mehdi Vaez Allaei, N. Provatas, A. Harju, K. R. Elder, and T. Ala-Nissila, Phys. Rev. B **94**, 035414 (2016).
[15] D. Taha, S. K. Mkhonta, K. R. Elder, and Z.-F. Huang, Phys. Rev. Lett. **118**, 255501 (2017).
[16] P. Hirvonen, Z. Fan, M. M. Ervasti, A. Harju, K. R. Elder, and T. Ala-Nissila, Sci. Rep. **7**, 4754 (2017).
[17] D. Taha, S. R. Dlamini, S. K. Mkhonta, K. R. Elder, and Z.-F. Huang, Phys. Rev. Mater. **3**, 095603 (2019).
[18] B. Waters and Z.-F. Huang, Acta Mater. **225**, 117583 (2022).
[19] P. Hirvonen, V. Heinonen, H. Dong, Z. Fan, K. R. Elder, and T. Ala-Nissila, Phys. Rev. B **100**, 165412 (2019).
[20] Z.-F. Huang, Phys. Rev. Mater. **6**, 074001 (2022).
[21] K. R. Elder, C. V. Achim, V. Heinonen, E. Granato, S. C. Ying, and T. Ala-Nissila, Phys. Rev. Mater. **5**, 034004 (2021).
[22] S. Zhou, J. Han, S. Dai, J. Sun, and D. J. Srolovitz, Phys. Rev. B **92**, 155438 (2015).
[23] K. R. Elder, N. Provatas, J. Berry, P. Stefanovic, and M. Grant, Phys. Rev. B **75**, 064107 (2007).
[24] Y. Guo, J. Qui, and W. Guo, Nanotechnology **27**, 505702 (2016).
[25] K. R. Elder, Z. Chen, K. L. M. Elder, P. Hivonen, S. K. Mkhonta, S.-C. Ying, E. Granato, Z.-F. Huang, and T. Ala-Nissila, J. Chem. Phys. **144**, 174703 (2016).
[26] K. R. Elder, C. V. Achim, E. Granato, S.-C. Ying, and T. Ala-Nissila, Phys. Rev. B **96**, 195439 (2017).
[27] F. Tumino, P. Carrozzo, L. Mascaretti, C. S. Casari, M. Passoni, S. Tosoni, C. E. Bottani, and A. L. Bassi, 2D Mater. **2**, 045011 (2015).
[28] C. Wu, M. S. J. Marshall, and M. R. Castell, J. Phys. Chem. C **115**, 8643 (2011).
[29] W. L. Ling, J. C. Hamilton, K. Thurmer, G. E. Thayer, J. de la Figuera, R. Q. Hwang, C. B. Carter, N. C. Bartelt, and K. F. McCarty, Surf. Sci. **600**, 1735 (2006).
[30] S. Dai, Y. Xiang, and D. J. Srolovitz, Nano Lett. **16**, 5923 (2016).
[31] R. Pushpa and S. Narasimhan, Phys. Rev. B **67**, 205418 (2003).
[32] M. Corso, L. Fernández, F. Schiller, and J. E. Ortega, ACS Nano **4**, 1603 (2010).
[33] H. Kumar, D. Er, L. Dong, J. Li, and V. B. Shenoy, Sci. Rep. **5**, 10872 (2015).
[34] J. A. Dantzig and M. Rappaz, *Solidification* (EPFL, Lausanne, 2009).